Ultrathin Hierarchical Porous Carbon Nanosheets for High-Performance Supercapacitors and Redox Electrolyte Energy Storage

Kolleboyina Jayaramulu, Deepak P. Dubal, Bhawna Nagar, Vaclav Ranc, Ondrej Tomanec, Martin Petr, Kasibhatta Kumara Ramanatha Datta, Radek Zboril, Pedro Gómez-Romero,* and Roland A. Fischer*

Dr. K. Jayaramulu, Prof. R. A. Fischer. Chair of Inorganic and Metal-Organic Chemistry Department of Chemistry and Catalysis Research Centre Technical University of Munich. 85748 Garching, Germany. E-mail: roland.fischer@tum.de

Dr. K. Jayaramulu, Dr. V. Ranc, O. Tomanec, Dr. M. Petr, Dr. K. K. R. Datta, Prof. R. Zboril Regional Centre of Advanced Technologies and Materials. Faculty of Science Palacky University Olomouc Šlechtitelů 27, 783 71 Olomouc, Czech Republic

Dr. D. P. Dubal, B. Nagar, Prof. P. Gómez-Romero. Catalan Institute of Nanoscience and Nanotechnology (ICN2) CSIC and the Barcelona Institute of Science and Technology Campus UAB, Bellaterra 08193, Barcelona, Spain. E-mail: pedro.gomez@icn2.cat

Dr. D. P. Dubal School of Chemical Engineering The University of Adelaide. Adelaide, South Australia 5005, Australia

ABSTRACT

The design of advanced high-energy-density supercapacitors requires the design of unique materials that combine hierarchical nanoporous structures with high surface area to facilitate ion transport and excellent electrolyte permeability. Here, shape-controlled 2D nanoporous carbon sheets (NPSs) with graphitic wall structure through the pyrolysis of metal–organic frameworks (MOFs) are developed. As a proof-of-concept application, the obtained NPSs are used as the electrode material for a supercapacitor. The carbon-sheet-based symmetric cell shows an ultrahigh Brunauer–Emmett– Teller (BET)-area-normalized capacitance of 21.4 μF cm^{-2} (233 F g^{-1}), exceeding other carbon-based supercapacitors. The addition of potassium iodide as redox-active species in a sulfuric acid (supporting electrolyte) leads to the ground-breaking enhancement in the energy density up to 90 Wh kg^{-1}, which is higher than commercial aqueous rechargeable batteries, maintaining its superior power density. Thus, the new material provides a double profits strategy such as battery-level energy and capacitor-level power density.

INTRODUCTION

The unique properties of supercapacitors (SCs) such as high power density, short charging/discharging time, and long cycle life make them highly attractive to a variety of applications such as portable electronics, electric devices, and vehicles.[1,2] However, the energy density of the SCs for these applications needs to be further enhanced.[3] Currently, carbon-based materials are the most successfully implemented SC electrodes because of their relatively low cost, good electrical conductivity, and high surface area. They are therefore ideal materials for the swift storage and release of energy.[4] Most of the capacitance arises from the formation of an electrical double layer (EDL) and the surface properties of carbon materials such as morphology, shape, dimension, and porosity.[5-8] The designing of superior carbon materials for high-performance SCs with tailored properties such as chemical stability, electrical conductivity, and large specific and functional surface area is a great challenge.[9-15]

The 2D porous carbon materials represent an emerging class of advanced functional materials showing potential as SC electrodes.[16] These 2D carbon nanosheets can provide high utilization of micropores in the interconnected hierarchical porous structure, high conductivity, and high specific surface area for charge storage.[17–19] Very recently, a few approaches have been devoted to the synthesis of such 2D porous carbon with greatly improved ion-transport properties.[20,21] Unfortunately, the multistep synthetic procedures used in these investigations are industrially unfeasible. Much effort has been dedicated to synthesize 2D nanoporous carbon sheets (NPSs) by an alternative, low-cost, and versatile route. Inorganic–organic hybrid porous metal–organic frameworks (MOFs) have been employed as sacrificial templates/precursors for synthesizing various hierarchical carbon materials profiting from high surface area, large pore volume, various metals/organic linkers, and their respectively tailored compositions.[22–27] Recently, Xu and co-workers reported the fabrication of 1D carbon nanorods by the morphology-persisted transformation of rod-shaped MOFs. In the next step, these carbon rods were converted to 2D graphene nanoribbons by a KOH-assisted sonochemical route. Nevertheless, the controlled

transformation of MOFs into 2D porous carbon nanosheets without any additional chemical etching step is still a great challenge. Herein, we report on a scalable strategy for the fabrication of shape-controlled 2D NPSs (designated as NPS-800) by the controlled carbonization of a specifically selected potassium-based MOF (Figure S1, Supporting Information) without any additional chemical etching agent.[27] The obtained material with a unique layered 2D carbon nanosheet mesostructure provides excellent specific surface area and pore volume that significantly enhances the charges stored at the electrode. The SC properties of NPS-800 electrodes are investigated in this work.

The incorporation of surface functionalities, and/or electroactive nanoparticles of transition metal oxides or conducting polymers are general strategies used to improve the performances of carbon-based SC.[28,29] Nevertheless such modifications may suffer from the unstable nature of these functionalities with cycling, degradation of the composites, or their high cost of implementation. An emerging approach is to implement the redox-active electrolytes to improve the specific capacitance of SCs.[30–34] The motivation is enhancing the capacitance and potential window (voltage) of aqueous electrolytes by shifting the oxygen evolution potential. The use of redox couples such as KI for I_2/I^- has been reported in conventional SCs (activated-carbon-based cells) with remarkable results. We transferred this concept to our NPS-800 material. The effect of the addition of redox-active species (KI in this particular case) in conventional aqueous H_2SO_4 electrolyte for a MOF-derived carbon
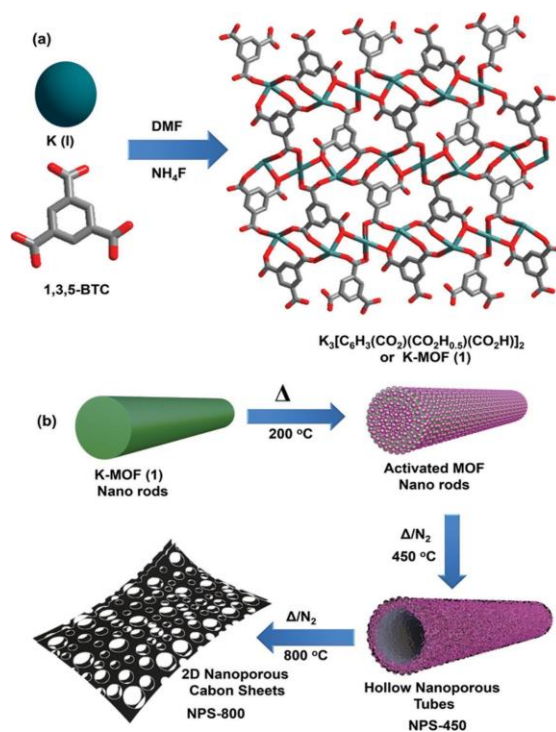
Figure 1. Materials synthesis: Schematic illustration of: a) synthesis of K-MOF rods under solvothermal conditions and b) morphologically controlled synthesis of 2D hierarchical NPSs NPS-800 derived from K-MOF under various carbonization conditions.

SCs was investigated for the first time. The combination of the excellent specific capacitance of NPS-800 with that provided by the redox reactions of the electrolyte leads to a spectacular increase in overall capacitance and consequently records high energy density of the device due to the extended voltage window and pseudocapacitance introduced by redox electrolyte.

The direct synthesis of 2D carbon sheets from a potassium-based MOF is illustrated in Figure 1a,b. The reaction of potassium nitrate and 1,3,5-benzene tricarboxylic acid in N,N-dimethyl formamide by the conventional solvothermal synthesis method resulted in the formation of $\{K_3[C_6H_3(CO_2)(CO_2H_{0.5}) (CO_2H)]_2\}(H_2O)_2$ (K-MOF) (Figure S1, Supporting Information).[35] The phase purity of the 2D K-MOF was confirmed by powder X-ray diffraction analysis (PXRD) (Figure S2, Supporting Information). Field-emission scanning electron microscopy (FESEM) images reveal rod-shaped K-MOF crystallites with sizes in the range between 0.1 and 1 µm (Figure 2a; Figures S3 and S4, Supporting Information). We

have deliberately chosen K-MOF as the self- sacrificing template to selectively synthesize NPSs by a facile, cost effective, shape-controlled approach. A first carbonization step at 450 °C in N_2 atmosphere yields the NPS-450 material (intermediate product) with the retention of rod-shaped hollow nanostructure (see Figure 2b; Figure S5, Supporting Information). In the second carbonization step, the rod-shaped potassium containing hollow carbon tubes (NPS-450) was trans- formed into 2D NPSs upon annealing at 800 °C (designated as NPS-800). Subsequently, the potassium-based impurities were removed by etching NPS-800 in 5 wt% HCl (hydrochloric acid), washing several times with water–ethanol mixture and drying the material at 100 °C (Figure S6b, Supporting Information).

The transmission electron microscopic (TEM) images of NPS-800 are presented in Figure 2c–f. The low magnified TEM image (Figure 2d) reveals the formation of a nanosheet carbon structure. These nanosheets exhibit a graphene-like layered structure with the domain
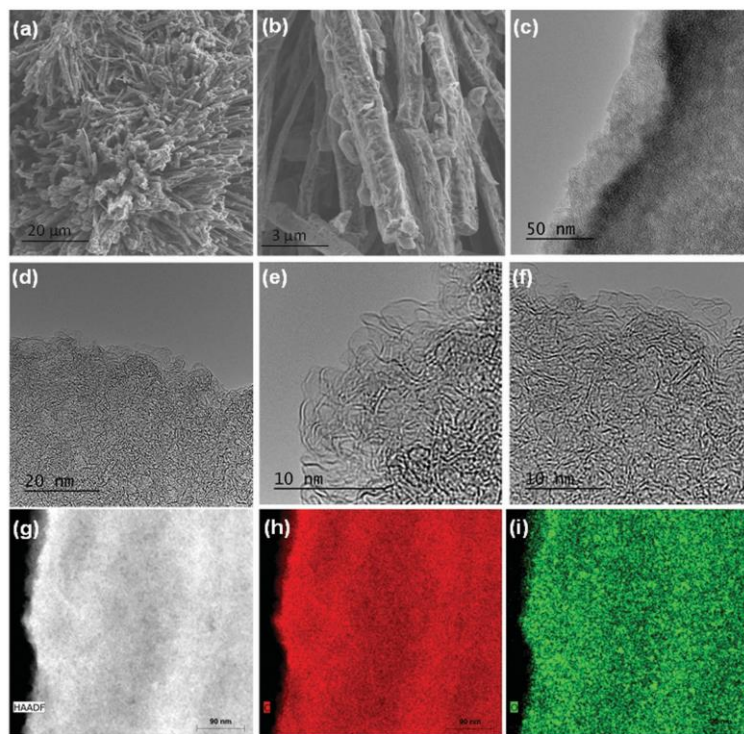

Figure 2. Microscopic imaging and elemental composition: SEM images of: a) nanorods of starting MOF precursor and b) nanoporous tubes of carbonized MOF at 450 °C (NPS-450). c–f) HRTEM images of an NPS-800 sample showing the nanosheet-like morphology with highly porous nature; g) HAADF image; and h, i) elemental mapping by EDX further confirms homogeneous distribution of carbon and oxygen throughout the sample.

size of few nanometers (around 5–10 nm) (see Figure 2e,f; Figure S6a, Supporting Information). It is further interesting to note that the nanosheets are clear and transparent, suggesting an ultrathin nature. Energy-dispersive X-ray spectroscopy (EDX) mapping further confirmed homogeneous distribution of carbon and oxygen as shown in Figure 2g–i. Thus, the results confirm the successful fabrication of 2D carbon nanosheets from 1D carbon nanorods without any chemical etching agent. This transformation of 1D nanorods to 2D nanosheets may be attributed to the presence of potassium cations from potassium carbonate (K_2CO_3) as reported in literature (the presence of potassium confirmed through EDX anal- ysis and presence of potassium carbonate determined through PXRD provided in Figures S7 and S8 in the Supporting Information).[27] A rationalization of the stepwise formation of NPSs from the MOF nanorod material is schematically illustrated in Figure S9 in the Supporting Information.

The composition and microstructure of the derived NPS-800 was characterized in detail and the data are discussed as follows. The PXRD pattern of the NPS-800 exhibits two broad peaks at 2θ = 11.5° and 24.3°, respectively (Figure 3a). The broad feature at 24.3° is assigned to the characteristic d_{002} graphitic peak of carbon materials. The Raman spectrum exhibits two intense bands at 1340 cm^{-1} (D-band) and 1583 cm^{-1} (G-band). The former band is attributed to disordered sp^2 carbon and the latter to ordered graphitic sp^2 carbon (Figure 3b). The examination of the D/G relative intensities indicates significant defects within the graphitic carbon environment.[36] Raman microscopic imaging shows a spatial distribution of D/G ratio over the assessed sample area fluctuating around the value D/G = 1. The chemigram (Figure S10, Supporting Information) contains regions with higher D/G ratio (red), and areas with minor defects and edges (blue). The composition, structural organization, and nature of coordination environment of NPS-800 were also characterized by X-ray photoelectron spectroscopy (XPS) (Figure 3c–e). The survey XPS spectrum clearly manifests the presence of two peaks corresponding to carbon (89.4%) and oxygen (10.6%). The C1s spectrum was deconvoluted into five peaks with binding energies 284.7, 285.8, 286.8, 287.8, and 289.1, which can be assigned to C-C (sp^2) (77.0%), C-C (sp^3) (14.1%), C-

O (5.9%), C-O (1.9%), and O-C-O (1.1%), respectively. The main peak at 284.7 eV originates from the sp^2 graphitic nature carbon (C-C sp^2) with 77%. In conclusion, Raman and XPS studies reveal that NPS-800 exhibits a dominant sp^2 carbon nature, quite expected for graphitic nano- structures, with few defects due to oxygen doping.
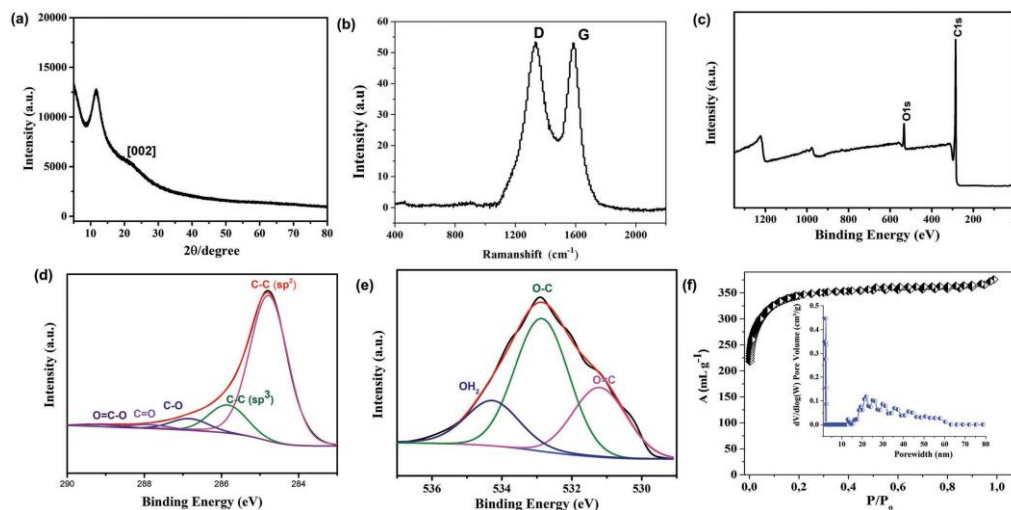

Figure 3. Microstructural characterization of NPS-800: a) PXRD pattern; b) Raman spectrum of graphitic carbon D- and G-band regions; c) XPS survey spectrum; d) XPS high-resolution spectra of C1s; e) O1s regions; and f) nitrogen adsorption–desorption isotherm; the inset shows the pore size distribution (1–70 nm) calculated from the nonlocal density functional theory (NLDFT) method.

High surface area with an open-pore structure is one of the keys to high-performance electrode materials for energy storage. In this sense, nitrogen adsorption–desorption studies and the corresponding pore size distribution analysis for an NPS-800 sample were performed and the data are displayed in Figure 3f. The derived BET and Langmuir surface areas are 1192 and 1678 $m^2\,g^{-1}$, respectively, with a large pore volume of 1.06 $cm^3\,g^{-1}$, which is high enough to facilitate the ion transportation.

Recently, multifunctional porous carbon materials with hierarchical porous structures have attracted considerable attention in electrochemical energy-storage and conversion devices. Thus, the encouraging microstructural data of NPS-800 imposed us to further investigate the

electrochemical performances of this new nanocarbon material. A standard three-electrode cell with H_2SO_4 (1M) electrolyte was used to estimate the working potential window. Figure 4a presents the cyclic voltammetry (CV) curves for the NPS-800 electrode in the potential window from −0.6 to +1.0 V (vs Ag/AgCl) with corresponding cathodic (0.0 to −0.6 V) and anodic (0.0 to +1.0 V) waves at a scan rate of 10 mV s^{-1}. Impressively, the NPS-800 electrode can be easily scanned in the both cathodic and anodic potential windows without any decomposition of the electrolyte as well as any other side reactions. This observation suggests that the estimated operational working potential range for carbon nanosheets could be up to 1.6 V. The shapes of CV curves are quasi-rectangular with small humps between 0.2 and 0.4 V, which suggests the inclusion of a pseudocapacitive behavior in addition to the EDL mechanism. The pseudocapacitance may occur due to the surface oxygen functional groups of NPS-800 as detected in the XPS analysis. As our proof-of-concept for practical realizations, we have further assembled symmetric supercapacitor cells with NPS-800 electrodes of the same areal masses (2 × 1.5 mg for each sample) in Swagelok cell design. Figure 4b displayed CV curves for the symmetric cell between 0 and 1.6 V at different scan rates from 5 to 100 mV s^{-1}. As expected, the cell shows excellent capacitive behavior with obvious rectangular CV curves. The maximum specific capacitance for NPS-800 electrode was found to be 233 F g^{-1} at a lowest scan rate of 5 mV s^{-1}, which was maintained to 145 F g^{-1} up to the high scan rate of 100 mV s^{-1}, suggesting good rate capability. The galvanostatic charge/discharge (GCD) curves exhibit triangular shapes that further approved the good capacitive behavior of the electrodes (Figure S11, Supporting Information). The specific capacitances for NPS-800-based cell were calculated from GCD curves. The obtained values are 70, 55, 49, 43, and 40 F g^{-1} (i.e., 42, 33, 29, 26, and 24 F cm^{-3}) at 0.7, 1.3, 2, 2.7, and 3.3 A g^{-1}, respectively. The cell shows good rate capability by retaining 58% initial capacitance after the increase in current density from 0.7 to 3.3 A g^{-1}. The decrease in capacitance at a high current density or high scan rate might be due to the insufficient time for charge transport through micro-/nanopores (diffusion limitation). The surface-area-normalized capacitance was calculated to be 21.35 μF cm^{-2}. This value is higher than that for any other carbon-based SC with the exception of holey graphene. This capacitance is

significantly higher compared with the best values reported for MOF-derived carbon materials known so far (Figure S12 and Table S1, Supporting Information).[27,37–41]
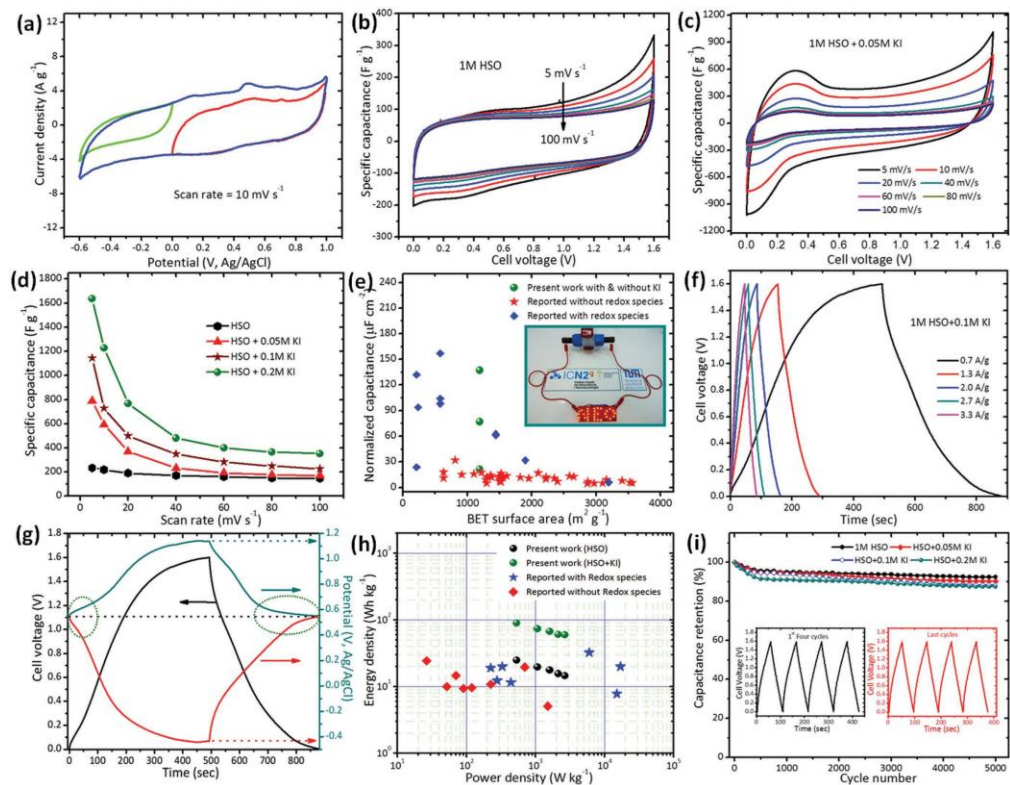

Figure 4. Electrochemical, supercapacitor, and battery properties for the symmetric NPS-800//NPS-800 cell: a) CV curve for the cell in wide 1.6 V window with CV curves measured for the electrodes in conventional three-electrode configuration with different working potential range showing the function of NPS-800 as positive as well as negative electrode. b,c) CV curves of the symmetric cell at different scan rates in conventional H_2SO_4 and in redox-active electrolytes (H_2SO_4 + 0.05 M KI), respectively. d) Variation of the specific capacitance of the cell with respect to scan rate. e) Comparison of areal capacitances among various EDLC materials normalized relative to their BET surface areas, the inset of figure shows practical demonstration of this device by lighting "31 LEDs" with word "NEO." f) GCD curves for the cell in redox electrolyte (H_2SO_4 + 0.1 M KI) at different current densities. g) GCD curves for the cell with the corresponding positive and negative electrode profiles with respect to Ag/AgCl reference electrode in redox-active electrolyte. h) Ragone plot for the cell with and without redox-active electrolyte and comparison of energy and power density values with the literature. i) Plots of capacity retention with cycle number for the cell at different concentrations of redox-active electrolyte.

Despite these excellent results, our new SC material still reveals comparably low energy density and hence immediate practical applications are limited. We advanced one step further and tested NPS-800 symmetric cells in a redox-active species containing electrolyte (named hybrid electrolytes) in order to realize advancement toward final device performance. For the successful implementation of redox electrolytes in SCs, the electrode material must be sufficiently porous and must be able to retain the redox species, particularly the product from the charging reaction, inside the pore system of the electrode material. The use of redox species in supporting electrolytes for EDL SCs has been studied earlier, for instance, using the I^-/I^- redox couple. [42,43] Most of the reports are based on activated carbon electrodes and/or cells. Herein, we are first time presenting the use of a redox-active electrolyte (here KI, I^-/I^- in the H_2SO_4 electrolyte) for MOF-derived nanoporous carbon peaks. Moreover, for higher concentrations of KI (such as 0.1 and 0.2 m), the shapes of CV curves are completely modified to a nonideal capacitive character; however, they cover an extra-large current area as compared with the pristine H_2SO_4 electrolyte (Figure S13, Supporting Information). This extra-large increase in the current density consequently improves the capacitance and energy density of the final device. The cell still sustains its large working potential window (1.6 V), suggesting double profit such as extended voltage window and extra-large capacitance. This capacitance may be attributed to the redox materials. Figure 4c shows CV curves for symmetric cell based reactions between the redox pairs of $3I^-/I_3^-$, $2I^-/I_2$, $2I_3^-/3I_2$, and I_2/IO_3^- [44] Figure 4d presents the linear variation of specific capacitances with scan rates at different concentrations of the KI additive. Remarkably, the specific capacitance of the NPS-800 electrode increases from 233 to 1636 F g^{-1} and that for a symmetric cell from 74 to 521 F g^{-1}, which is almost 7-fold enhancement at 0.2 M KI addition in H_2SO_4. This huge increase in the specific capacitance of the electrode as well as the cell corresponds to the redox activities introduced in the parent H_2SO_4 electrolyte. The cell with redox-active electrolyte shows less capacity retention (21%) as compared with that of pristine electrolyte; however, the capacitance is still 50% larger (350 F g^{-1} for electrode

and 111 F g^{-1} for cell). The electrochemical properties of the NPS-800 cell derived from CV and GCD curves are com- piled in Tables S2 and S3 in the Supporting Information, respectively. The redox peaks become more significant and prominent with the scan rate, indicating excellent electrochemical reversibility of carbon nanosheet electrodes. The redox peaks slightly shift with scan rate, suggesting more efficient electrochemical reactions at electrode/electrolyte interface (Figure S13, Sup- porting Information). The area-normalized capacitance was calculated for our system and compared with previously reported data. The reference data of BET area-normalized capacitance were calculated from the data given in corresponding reports. The area-normalized capacitance was remarkably increased from 19 to 137.3 µF cm−2, which is superior compared with the previously reported values (see Figure 4e). The capacitances achieved in the present investigation are higher than those values reported for other carbon-based mate-rials (Table S4, Supporting Information). [45–49] The results assure the positive effect of KI addition on the electrochemical properties of carbon nanosheet electrodes through pseudo-capacitive reactions. The practical demonstration of NPS-800 symmetric cell with 0.2 M KI + H2SO4 electrolyte is shown in the inset of Figure 4e. Thirty-one LEDs are illuminated for almost 90 s after a full-charging of 10 s, suggesting maintained energy output at a rapid charge. In summary, the NPS-800 turned out as almost perfect electrode material to be used in such kind of redox electrolyte-based SCs. This is assigned to the specific nanostructure combining high surface area and hierarchical nanoporous nature, which ensures effective electro- and/or chemisorption and charge transport.

The GCD curves were recorded for NPS-800 cell at different current densities and with various KI doping concentrations. Figure 4f shows the GCD curves of the cell in 0.1 M KI-added H$_2$SO$_4$ electrolyte. Notably, the GCD curves are switched from their original triangular shape, indicating the contribution from potential dependent redox reactions. These observations are strongly supported by the CV measurements. The cell exhibits a prolonged discharge time in KI-doped H2SO4 electrolyte than that for the parent H2SO4 electrolyte, signifying a considerable increase in the specific capacitance (Figure S14, Supporting Information). The discharge time and consequently the specific capacitance increases linearly with KI concentration. The volumetric capacitance of the cell is significantly improved from 42 to 151 F cm−3 at 0.7 A g−1 current density (the volumetric capacitances were calculated

using volume of the device). Simultaneous experiments in two- and three-electrode designs allow us to evaluate the potential distribution across each electrode during GCD cycle. Figure 4g shows the GCD curve (cell voltage, left Y-axis) and the corresponding potential distribution across the positive and negative electrodes versus Ag/AgCl in 0.1 M KI-added H2SO4 electrolyte (right Y-axis). The GCD curves for both positive and negative electrodes are ideally triangular in the case of pristine H_2SO_4 electrolyte (Figure S15, Supporting Information). On the contrary, the addition of redox-active species into the parent electrolyte completely alters the behavior of both electrodes. At the beginning of charging and end of discharge curves of both positive and negative electrodes, a small variation in potential with time is observed (Figure 4g). Afterward, charge/discharge curves for positive electrode are nontriangular, indicating the presence of faradaic reactions due to the iodide redox couple while the negative electrode follows a triangular shape. This observation suggests that initially both electrodes behave like battery while in the next step, one electrode (negative) is working like a capacitor and the other (positive) like a bat- tery, thereby getting double profit. The potential is asymmetrically distributed across the positive and negative electrodes. The positive electrode swings between +0.55 and +1.15 while that the negative electrode between +0.55 and −0.45 V (vs Ag/AgCl).

The energy and power density are the key data for practical applicability of energy-storage devices. Figure 4h shows the energy and power density values for NPS-800 cell with and without KI-doped H2SO4 electrolytes. The values for other carbon-based symmetric cells are provided for comparison. The cell exhibits an energy density of 24.8 Wh kg^{-1} (14.93 mWh cm^{-3}) at a power density of 533 W kg^{-1} (320 mW cm^{-3}) in the pris- tine H2SO4 electrolyte, which is considerably higher than previously reported values.[50–53] The energy and power density data of the NPS-800 cell are shown in Table S5 in the Sup- porting Information. This high energy density is attributed to the unique porous nanosheet-like morphology with chemical functionalities, which provides a large number of electrochemically active sites. The energy density was further increased to 89.7 Wh kg^{-1} (53.8 Wh cm^{-3}) for KI-modified H2SO4 electrolyte maintaining the same power density. This measured value is the highest energy density reported for carbon-based mate- rials

and comparable to typical commercial devices (Table S6, Supporting Information), such as rechargeable lithium batteries (30–55 Wh kg^{-1}), Pb-acid batteries (30–45 Wh kg^{-1}), and Ni/MH batteries (60–120 Wh kg^{-1}).[54,55]

The long-term cycling stability for NPS-800 cell was tested in pristine (H$_2$SO$_4$) and redox-active-modified electrolytes (KI + H$_2$SO$_4$) and shown in Figure 4i. The cycle stability of the cell is not as good as that in the parent H$_2$SO$_4$ electrolyte. This observation is rationalized as follows. Initially, the redox iodide species in the electrolyte are adsorbed at the internal and external surfaces of NPS-800 electrode and undergo electron transfer reactions. These intense redox reactions involve the recombination of I$_3$/I$^-$, I$_2$/I$^-$, and I$_2$/I$_3^-$ redox couples toward I$_5^-$, which are not fully reversible in the supporting electrolyte (H2SO4). Therefore, the NPS-800 cell showed lower cycling stability in KI-modified H2SO4 than that for parent H2SO4 electrolyte. As seen from Figure 4i, the cell retains 92% of initial capacitance over 5000 cycles in H2SO4 electrolyte, which is slightly higher than that in the redox active KI-modified H2SO4 electrolyte (86.2%). Nevertheless, due to the considerable advancement in the specific capacitance in KI-modified electrolyte, the actual specific capacitance values of NPS-800 in the redox-active electrolytes are still higher than that in the pristine H2SO4 electrolyte even after 5000 cycles.

In order to provide deeper insights into the involved mechanisms, we have performed ex situ XPS analysis of positive and negative electrodes at different conditions such as after full charge and full discharge states with and without KI electrolyte as shown in Figure 5a. The XPS spectra for positive and negative electrodes in H$_2$SO$_4$ electrolyte suggest the presence of C, O, and S peaks, which hint to SO$_4$$^{2-}$ species. On the other hand, when the cell is charged to 1.6 V in KI + H$_2$SO$_4$ electrolyte, XPS shows the presence of iodine in both the electrodes. The apparent two I3d peaks located at 619.4 and 631.0 eV can be assigned to I3d$_{5/2}$ and I3d$_{3/2}$ states, respectively. The signals of I3d$_{5/2}$ at 619.4 correspond to bonding between carbon and iodine species such as C-I and C-I$^+$-C as the oxidation products of I$^-$ during the reaction process.[56] This proves our first claim that during the charging process, positive electrodes start to behave like a battery within the voltage range of +0.5 to +0.7 V, (vs Ag/AgCl) as

shown in Figure 4g, where the potentials remain almost constant with time due to the involvement of faradaic charge-storing mechanism. Figure 5c presents the amount of iodine species found in both electrodes. Later, when the cell is completely discharged (0 V), ex situ XPS shows a strong peak of I3d for the positive electrode, suggesting the presence of more iodine species than that for the negative electrode (see Figure 5b). This might be explained as follows. As seen in Figure 4g, charges from the Faradaic reaction of iodine species are compensated in the positive electrodes by two different energy-storage mechanisms: (i) electrochemical reaction of iodine and (ii) the charging of the electric double layer. Due to these different charge-storing mechanisms, the **NPS-800** symmetric cell behaves as a hybrid system. Thus, from a quantitative point of view, the incorporation of iodine species significantly increases the capacitance of whole cell. Hence, the outstanding enhancement in the final cell based on the **NPS-800** electrodes is achieved by synergetic integration of the two above discussed mechanisms. It is further interesting to note that there is no change in the nanostructure of **NPS-800** electrodes after first charge and discharge in 0.2 M KI-doped H_2SO_4 electrolyte, which is evidenced from the TEM images shown in Figure 5d–f. In addition, the EDX data recorded during scanning electron microscopy (SEM) imaging confirm the existence of iodide species on the surface of the electrodes (see Figure S16, Supporting Information). The reasons for this breakthrough advancement in the electrochemical performances of nanocarbon-based SCs are summarized as follows: (i) the design of unique nanoporous, wrapped paper-like nanosheets with high surface area and large pore size, which significantly improve the electrode/electrolyte interface contacts and shorten the diffusion lengths. (ii) Carbon nanosheets offer large amount of electroactive, chemically functional sites and provide more sustainability during the long-term charge/discharge cycles. (iii) A wide potential working window (1.6 V) caused by the combination of carbon nanosheets with redox-active species considerably improves energy density of the SCs.
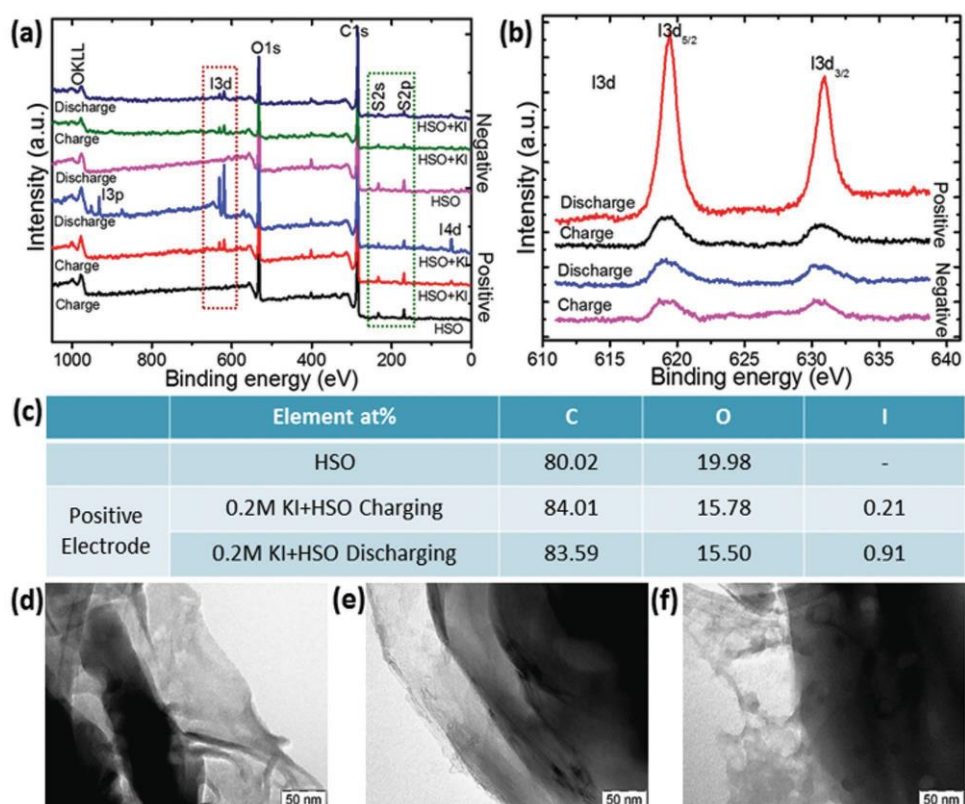
Figure 5. Characterization after electrochemical cycling. a) Ex situ full XPS spectra for positive and negative NPS-800 electrodes after full charging and full discharging with and without KI electrolyte, confirming the presence of iodine attached to the carbon. b) Magnified view of ex situ XPS of I3d suggesting the higher content of iodine species in positive electrode after discharge. c) Table showing the compositions of the electrode materials after full charge and discharge states. d–f) TEM images of the electrodes initial state, after full charge and discharge states, respectively, suggesting no change in the nano-/mesostructure.

In conclusion, high-surface-area hierarchical carbon nanosheets with controlled porosity derived from a suitably chosen MOF as self-sacrificial precursor and template have been successfully implemented for high voltage (1.6 V) SCs. The fabricated NPS-800 electrode provides an ultrahigh BET surface-area-normalized capacitance of 21.4 μF cm^{-2}. This value is remarkably superior to any other MOF-derived carbon material. The addition of redox-active species (KI) in a conventional H_2SO_4 electrolyte leads to unique further enhancement in the energy density of the symmetric cell maintaining their high power density. The obtained record high energy density ($\approx$90 Wh kg^{-1}) for a carbon-based

supercapacitor material is comparable to commercial aqueous rechargeable batteries. Thus, our investigation provides a novel guideline for the further development of carbon-based energy-storage systems with battery-level energy and capacitor-level power density.

REFERENCES

[1] P. Simon, Y. Gogotsi, *Nat. Mater.* 2008, *7*, 845.

[2] D. P. Dubal, O. Ayyad, V. Ruiz, P. Gomez-Romero, *Chem. Soc. Rev.* 2015, *44*, 1777.

[3] P. Simon, Y. Gogotsi, B. Dunn, *Science* 2014, *343*, 1210.

[4] H. Jiang, P. S. Lee, C. Li, *Energy Environ. Sci.* 2013, *6*, 41.

[5] Y. Wang, Y. Song, Y. Xia, *Chem. Soc. Rev.* 2016, *45*, 5925.

[6] F. Béguin, V. Presser, A. Balducci, E. Frackowiak, *Adv. Mater.* 2014, *26*, 2219.

[7] M. Sevilla, R. Mokaya, *Energy Environ. Sci.* 2014, *7*, 1250.

[8] J. Wang, S. Kaskel, *J. Mater. Chem.* 2012, *22*, 23710.

[9] D. N. Futaba, K. Hata, T. Yamada, T. Hiraoka, Y. Hayamizu, Y. Kakudate, O. Tanaike, H. Hatori, M. Yumura, S. Iijima, *Nat. Mater.* 2006, *5*, 987.

[10] J. Gamby, P. L. Taberna, P. Simon, J. F. Fauvarque, M. Chesneau, *J. Power Sources* 2001, *101*, 109.

[11] Y. Gogotsi, A. Nikitin, H. Ye, W. Zhou, J. E. Fischer, B. Yi, H. C. Foley, M. W. Barsoum, *Nat. Mater.* 2003, *2*, 591.

[12] J. Chmiola, G. Yushin, Y. Gogotsi, C. Portet, P. Simon, P. L. Taberna, *Science* 2006, *313*, 1760.

[13] J. Huang, B. G. Sumpter, V. Meunier, *Chem. - Eur. J.* 2008, *14*, 6614. [14] H. Ji, X. Zhao, Z. Qiao, J. Jung, Y. Zhu, Y. Lu, L. L. Zhang, A. H. MacDonald, R. S. Ruoff, *Nat. Commun.* 2014, *5*, 3317.

[15] G. Chen, W. Zhai, Z. Wang, J. Yu, F. Wang, Y. Zhao, G. Li, *Mater. Res. Bull.* 2015, *72*, 204.

[16] D.-W. Wang, F. Li, M. Liu, G. Q. Lu, H.-M. Cheng, *J. Phys. Chem. C* 2008, *112*, 9950.

[17] Z. Fan, Y. Liu, J. Yan, G. Ning, Q. Wang, T. Wei, L. Zhi, F. Wei, *Adv. Energy Mater.* 2012, *2*, 419.

[18] J. Luo, H. D. Jang, J. Huang, *ACS Nano* 2013, *7*, 1464.

[19] J. Xu, Q. Gao, Y. Zhang, Y. Tan, W. Tian, L. Zhu, L. Jiang, *Sci. Rep.* 2014, *4*, 5545.

[20] K. Yuan, T. Hu, Y. Xu, R. Graf, G. Brunklaus, M. Forster, Y. Chen, U. Scherf, *ChemElectroChem* 2016, *3*, 822.

[21] X. Zheng, J. Luo, W. Lv, D.-W. Wang, Q.-H. Yang, *Adv. Mater.* 2015, *27*, 5388.

[22] B. Liu, H. Shioyama, T. Akita, Q. Xu, *J. Am. Chem. Soc.* 2008, *130*, 5390.

[23] J. Tang, R. R. Salunkhe, J. Liu, N. L. Torad, M. Imura, S. Furukawa, Y. Yamauchi, *J. Am. Chem. Soc.* 2015, *137*, 1572.

[24] W. Xia, A. Mahmood, R. Zou, Q. Xu, *Energy Environ. Sci.* 2015, *8*, 1837.

[25] J.-K. Sun, Q. Xu, *Energy Environ. Sci.* 2014, *7*, 2071.

[26] K. Jayaramulu, K. K. R. Datta, K. Shiva, A. J. Bhattacharyya, M. Eswaramoorthy, T. K. Maji, *Microporous Mesoporous Mater.* 2015, *206*, 127.

[27] P. Pachfule, D. Shinde, M. Majumder, Q. Xu, *Nat. Chem.* 2016, *8*, 718.

[28] J. P. Paraknowitsch, A. Thomas, *Energy Environ. Sci.* 2013, *6*, 2839. [29] Y. Shi, L. Peng, Y. Ding, Y. Zhao, G. Yu, *Chem. Soc. Rev.* 2015, *44*, 6684. [30] X. Zhao, B. M. Sanchez, P. J. Dobson, P. S. Grant, *Nanoscale* 2011, *3*, 839.

[31] S. Roldán, C. Blanco, M. Granda, R. Menéndez, R. Santamaría, *Angew. Chem., Int. Ed.* 2011, *50*, 1699.

[32] E. Frackowiak, K. Fic, M. Meller, G. Lota, *ChemSusChem* 2012, *5*, 1181.

[33] Y. Xu, Z. Lin, X. Zhong, X. Huang, N. O. Weiss, Y. Huang, X. Duan, *Nat. Commun.* 2014, *5*, 4554.

[34] D. P. Dubal, J. Suarez-Guevara, D. Tonti, E. Enciso, P. Gomez- Romero, *J. Mater. Chem. A* 2015, *3*, 23483.

[35] M. K. Kim, V. Jo, D. W. Lee, I.-W. Shim, K. M. Ok, *CrystEngComm* 2010, *12*, 1481.

[36] A. C. Ferrari, J. Robertson, *Phys. Rev. B* 2000, *61*, 14095.

[37] D. Sheberla, J. C. Bachman, J. S. Elias, C.-J. Sun, Y. Shao-Horn, M. Dinca, *Nat. Mater.* 2017, *16*, 220.

[38] C. Young, R. R. Salunkhe, J. Tang, C.-C. Hu, M. Shahabuddin, E. Yanmaz, M. S. A. Hossain, J. H. Kim, Y. Yamauchi, *Phys. Chem. Chem. Phys.* 2016, *18*, 29308.

[39] R. R. Salunkhe, Y. Kamachi, N. L. Torad, S. M. Hwang, Z. Sun, S. X. Dou, J. H. Kim, Y. Yamauchi, *J. Mater. Chem. A* 2014, *2*, 9848.

[40] A. J. Amali, J.-K. Sun, Q. Xu, *Chem. Commun.* 2014, *50*, 1519.

[41] X. Cao, C. Tan, M. Sindoro, H. Zhang, *Chem. Soc. Rev.* 2017, *46*, 2660.

[42] J. Hu, H. Wang, Q. Gao, H. Guo, *Carbon* 2010, *48*, 3599.

[43] W. Xia, R. Zou, L. An, D. Xia, S. Guo, *Energy Environ. Sci.* 2015, *8*, 568.

[44] W. Xia, A. Mahmood, R. Zou, Q. Xu, *Energy Environ. Sci.* 2015, *8*, 1837.

[45] Y. Liang, J. Wei, Y. X. Hu, X. F. Chen, J. Zhang, X. Y. Zhang, S. P. Jiang, S. W. Tao, H. T. Wang, *Nanoscale* 2017, *9*, 5323.

[46] Q. Lu, M. W. Lattanzi, Y. Chen, X. Kou, W. Li, X. Fan, K. M. Unruh, J. G. Chen, J. Q. Xiao, *Angew. Chem., Int. Ed.* 2011, *50*, 6847.

[47] Y. Ren, A. R. Armstrong, F. Jiao, P. G. Bruce, *J. Am. Chem. Soc.* 2010, *132*, 996.

[48] B. Liu, H. Shioyama, H. Jiang, X. Zhang, Q. Xu, *Carbon* 2010, *48*, 456.

[49] L. Radhakrishnan, J. Reboul, S. Furukawa, P. Srinivasu, S. Kitagawa, Y. Yamauchi, *Chem. Mater.* 2011, *23*, 1225.

[50] L. Zhang, F. Zhang, X. Yang, G. Long, Y. Wu, T. Zhang, K. Leng, Y. Huang, Y. Ma, A. Yu, Y. Chen, *Sci. Rep.* 2013, *3*, 1408.

[51] Y. Zhu, S. Murali, M. D. Stoller, K. J. Ganesh, W. Cai, P. J. Ferreira, A. Pirkle, R. M. Wallace, K. A. Cychosz, M. Thommes, D. Su, E. A. Stach, R. S. Ruoff, *Science* 2011, *332*, 1537.

[52] Y. Xu, Z. Lin, X. Zhong, X. Huang, N. O. Weiss, Y. Huang, X. Duan, *Nat. Commun.* 2014, *5*, 4554.

[53] A. Izadi-Najafabadi, S. Yasuda, K. Kobashi, T. Yamada, D. N. Futaba, H. Hatori, M. Yumura, S. Iijima, K. Hata, *Adv. Mater.* 2010, *22*, E235-E241.

[54] A. Burke, *Electrochim. Acta* 2007, *53*, 1083.

[55] P. G. Campbell, M. D. Merrill, B. C. Wood, E. Montalvo, M. A. Worsley, T. F. Baumann, J. Biener, *J. Mater. Chem. A* 2014, *2*, 17764.

[56] L. Demarconnay, E. Raymundo-Piñero, F. Béguin, *Electrochem.Commun.* 2010, *12*, 1275.